# Photoacoustic imaging of prostate brachytherapy seeds

**Jimmy L. Su,**[1,3] **Richard R. Bouchard,**[1,2,3] **Andrei B. Karpiouk,**[1]
**John D. Hazle,**[2] **and Stanislav Y. Emelianov**[1,2,*]

[1]*Department of Biomedical Engineering, University of Texas at Austin, Austin, TX 78712, USA*
[2]*Department of Imaging Physics, MD Anderson Cancer Center, Houston, TX 77030, USA*
[3]*Contributed equally*

*\*emelian@mail.utexas.edu*

**Abstract:** Brachytherapy seed therapy is an increasingly common way to treat prostate cancer through localized radiation. The current standard of care relies on transrectal ultrasound (TRUS) for imaging guidance during the seed placement procedure. As visualization of individual metallic seeds tends to be difficult or inaccurate under TRUS guidance, guide needles are generally tracked to infer seed placement. In an effort to improve seed visualization and placement accuracy, the use of photoacoustic (PA) imaging, which is highly sensitive to metallic objects in soft tissue, was investigated for this clinical application. The PA imaging properties of bare (i.e., embedded in pure gelatin) and tissue-embedded (at depths of up to 13 mm) seeds were investigated with a multi-wavelength (750 to 1090 nm) PA imaging technique. Results indicate that, much like ultrasonic (US) imaging, an angular dependence (i.e., seed orientation relative to imaging transducer) of the PA signal exists. Despite this shortcoming, however, PA imaging offers improved contrast, over US imaging, of a seed in prostate tissue if sufficient local fluence is achieved. Additionally, although the PA signal of a bare seed is greatest for lower laser wavelengths (e.g., 750 nm), the scattering that results from tissue tends to favor the use of higher wavelengths (e.g., 1064 nm, which is the primary wavelength of Nd:YAG lasers) when the seed is located in tissue. A combined PA and US imaging approach (i.e., PAUS imaging) shows strong potential to visualize both the seed and the surrounding anatomical environment of the prostate during brachytherapy seed placement procedures.

**OCIS codes:** (170.5120) Photoacoustic imaging; (170.7170) Ultrasound; (170.1610) Clinical applications; (170.7230) Urology; (170.3660) Light propagation in tissues; (110.0113) Imaging through turbid media.

---

**References and links**

1. A. Jemal, R. Siegel, J. Xu, and E. Ward, "Cancer statistics, 2010," CA-Cancer J. Clin. p. caac.20073 (2010).
2. S. Nag, D. Beyer, J. Friedland, P. Grimm, and R. Nath, "American brachytherapy society (abs) recommendations for transperineal permanent brachytherapy of prostate cancer," Int. J. Radiat. Oncol. **44**, 789–799 (1999).
3. Z. Wei, M. Ding, D. Downey, and A. Fenster, "3d trus guided robot assisted prostate brachytherapy," in "Medical Image Computing and Computer-Assisted Intervention MICCAI 2005," , vol. 3750 of *Lecture Notes in Computer Science*, J. Duncan and G. Gerig, eds. (Springer Berlin / Heidelberg), pp. 17–24.
4. M. P. R. V. Gellekom, M. A. Moerland, J. J. Battermann, and J. J. W. Lagendijk, "MRI-guided prostate brachytherapy with single needle method–a planning study," Radiother. Oncol. **71**, 327–332 (2004).

5. J. Xue, F. Waterman, J. Handler, and E. Gressen, "Localization of linked 125i seeds in postimplant trus images for prostate brachytherapy dosimetry," Int. J. Radiat. Oncol. **62**, 912–919 (2005).
6. B. J. Davis, R. R. Kinnick, M. Fatemi, E. P. Lief, R. A. Robb, and J. F. Greenleaf, "Measurement of the ultrasound backscatter signal from three seed types as a function of incidence angle: application to permanent prostate brachytherapy," Int. J. Radiat. Oncol. **57**, 1174–1182 (2003).
7. B. H. Han, K. Wallner, G. Merrick, W. Butler, S. Sutlief, and J. Sylvester, "Prostate brachytherapy seed identification on post-implant trus images," Med. Phys. **30**, 898–900 (2003).
8. S. Nath, Z. Chen, N. Yue, S. Trumpore, and R. Peschel, "Dosimetric effects of needle divergence in prostate seed implant using 125I and 103Pd radioactive seeds," Med. Phys. **27**, 1058–1066 (2000).
9. S. Prahl, "Optical properties spectra compiled by Scott Prahl," http://omlc.ogi.edu/spectra/.
10. B. Karlsson, C. G. Ribbing, A. Roos, E. Valkonen, and T. Karlsson, "Optical properties of some metal oxides in solar absorbers," Phys. Scr. **25**, 826 (1982).
11. M. Xu and L. V. Wang, "Photoacoustic imaging in biomedicine," Rev. Sci. Instrum. **77**, 041101 (2006).
12. J. Su, A. Karpiouk, B. Wang, and S. Emelianov, "Photoacoustic imaging of clinical metal needles in tissue," J. Biomed. Opt. **15**, 021309 (2010).
13. S. Nag, J. P. Ciezki, R. Cormack, S. Doggett, K. DeWyngaert, G. K. Edmundson, R. G. Stock, N. N. Stone, Y. Yu, and M. J. Zelefsky, "Intraoperative planning and evaluation of permanent prostate brachytherapy: report of the american brachytherapy society," Int. J. Radiat. Oncol. **51**, 1422–1430 (2001).
14. E. Lee and M. Zaider, "Intraoperative dynamic dose optimization in permanent prostate implants," Int. J. Radiat. Oncol. **56**, 854–861 (2003).
15. T. Varghese and J. Ophir, "An analysis of elastographic contrast-to-noise ratio," Ultrasound Med. Biol. **24**, 915–924 (1998).
16. T. Svensson, E. Alerstam, M. Einarsdóttír, K. Svanberg, and S. Andersson-Engels, "Towards accurate in vivo spectroscopy of the human prostate," J. Biophotonics **1**, 200–203 (2008).
17. H. Hricak, R. Jeffrey, G. Dooms, and E. Tanagho, "Evaluation of prostate size: a comparison of ultrasound and magnetic resonance imaging," Urol. Radiol. **9**, 1–8 (1988).
18. American National Standards Institute, *ANSI Z136.1-2007 American national standard for safe use of lasers* (2007).
19. K. Homan, S. Kim, Y. S. Chen, B. Wang, S. Mallidi, and S. Emelianov, "Prospects of molecular photoacoustic imaging at 1064 nm wavelength," Opt. Lett. **35**, 2663–2665 (2010).
20. J. F. Corbett, J. J. Jezioranski, J. Crook, T. Tran, and I. W. T. Yeung, "The effect of seed orientation deviations on the quality of 125 i prostate implants," Phys. Med. Biol. **46**, 2785 (2001).

## 1. Introduction

In 2010, prostate cancer was the second most common cancer among men, with 217,730 cases that year alone [1]. The use of brachytherapy seeds, metal implants which deliver localized radiation therapy, is becoming a common treatment option for prostate cancer [2]. Brachytherapy seeds are typically minute (0.8 x 4.5 mm) capsules of stainless steel or titanium that are filled with a radioisotope, most commonly iodine-125 or palladium-103. Implantation is achieved by injecting the seeds (typically, 70-150 of them) into a cancerous prostate by way of metal guide needles that are inserted through a patient's perineum according to a preestablished treatment plan. Currently, the standard of care for the guidance of brachytherapy seed implantation is transrectal ultrasound (TRUS) [3], which can gain imaging access to the prostate given the gland's adjacency to the rectal wall and its modest size, with a mean±SD diameter (i.e., height or width dimension), according to a study by Hricak *et al.*, of 4.3±1.0 cm for men ($n = 15$) aged 52-67 years [17]. Since visualization of the small seeds can be difficult, the ultrasound-derived position of the needles - and not the seeds themselves - is often relied upon to infer seed placement [4]. Acoustic shadowing from microcalcifications, off-axis seed placement (i.e., where the ultrasound beam widens), and placement in specific regions of the prostate (e.g., in the periprostatic region, which can have a similar echogenicity to the seeds) can make visualization of seeds with TRUS difficult [5]. Additionally, the acoustic signal generated by a seed is highly dependent on its orientation, with seeds oriented with their long axis perpendicular to the beam more apt to being detected [6]. Given the difficulty in accurately visualizing seeds with TRUS, CT imaging is typically utilized for post-implant dosimetric evaluations [7]. Seed placement that deviates from the dosimetric treatment plan can result in underdosed cancerous regions,

requiring postoperative dose corrections through external-beam radiation therapy [3]. Needle deflections of only 5° from the insertion angle decrease the minimum target dose by 10%, thus increasing the tumor-cell survival rate by a factor of 200 [8].
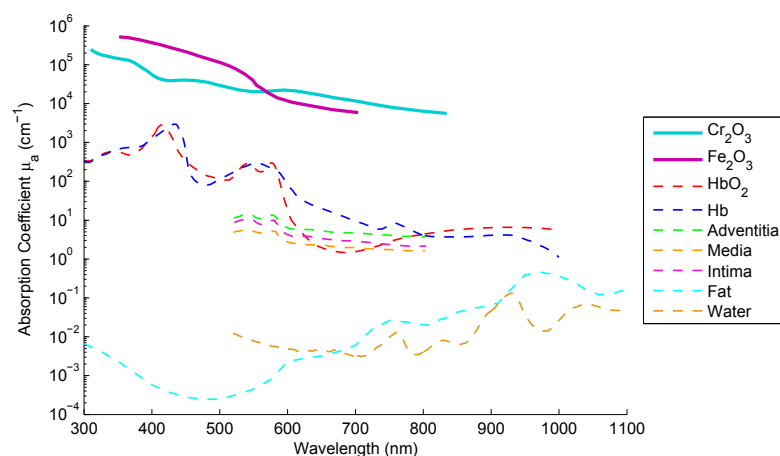


Fig. 1. Optical absorption spectra of various tissue constituents *in vivo* [9]. Also shown is optical absorption coefficient of stainless steel 316L; the surface passivation layer of stainless steel is primarily $Cr_2O_3$, which dominates in generation of PA effect, while stainless steel core is $Fe_2O_3$ [10].

    Photoacoustic (PA) imaging is an imaging technique in which tissue is irradiated with nanosecond pulses of low-energy laser light [11]. Through the processes of optical absorption followed by thermoelastic expansion, broadband ultrasonic (US) acoustic waves are generated within the irradiated volume. Using an ultrasound transducer, acoustic waves can be detected and spatially resolved to provide an image that is related to the local optical absorption of tissue constituents. Metals experience an optical absorption that is orders of magnitude greater than that experienced by soft tissue (Fig. 1), and thus PA imaging provides excellent contrast of metals embedded in soft tissue. Relying on this phenomenon, PA imaging has already been demonstrated to improve the image contrast of clinical metal needles in excised tissue specimens [12]. Generally, PA imaging cannot offer the soft tissue contrast afforded by US imaging. Since an ultrasound transducer is used in PA imaging, however, it is possible to obtain co-registered PA and US images. Consequently, a combined PA and US (PAUS) imaging approach will not only improve needle visualization during a seed implantation procedure, but it also promises to allow for the reliable visualization of the conventional, non-modified seeds themselves. Such a capability would improve adherence to a patient's dosimetric treatment plan, may allow for intraoperative dynamic dose optimization, and could obviate the need for costly and ionizing CT-based post-implant evaluations and external-beam radiation corrections [13, 14].

## 2. Materials and Methods

To test the feasibility of using PAUS imaging to visualize brachytherapy seeds, several imaging studies were conducted using non-reactive, stainless steel, iodine-125 brachytherapy seeds (IsoAid LLC, Port Richey, FL). PAUS imaging studies were performed using a Cortex ultrasound imaging system (Winprobe Corp., North Palm Beach, FL) that was interfaced with a 7-MHz center frequency, 14-mm-wide, 128-element linear array transducer (L7, Acuson Corp., Mountain View, CA). An Nd:YAG pump laser (Quanta-Ray PRO-290-10, Newport Corp.,

Irvine, CA) with OPO laser output (premiScan/BB 650 OPO, Newport Corp., Irvine, CA) and a nominal pulse width of 5 ns was synchronized to the ultrasound acquisition system to optically illuminate the sample in which the seed was embedded. The imaging system was capable of acquiring co-registered PA and US images to facilitate PAUS imaging.

In the first experiment (i.e., the "angular dependence experiment"), the angular dependence of the US and PA signals on seed orientation was investigated. A non-reactive brachytherapy seed was embedded in 8% gelatin at 45° relative to the horizontal ("Side View" of Fig. 2). In an effort to evaluate the seed independently from background influences, acoustic/optical scatterers were not added to the gelatin phantom. A mechanical stage was configured to rotate the transducer from 45° to 135° (relative to the same horizontal reference) in 15° increments. This allowed the long axis of the seed to be imaged at angles from 0° to 90° relative to the transducer face. Both the gelatin phantom and the transducer face were immersed in deionized water to provide acoustic coupling. The seed was placed at the fulcrum of the transducer's rotation to ensure that the seed remained in approximately the same location in the transducer's field of view through the 90° rotation. The laser was operated at 800 nm for PA imaging and was delivered to the sample using a single optical fiber; the fiber had a diameter of 1.5 mm, an NA of 0.39, and was positioned at an oblique angle to the US beam axis ("Front View" of Fig. 2). During the experiment, the laser irradiation position was not altered - the optical fiber and seed were held fixed while only the transducer was rotated - in order to demonstrate that signal changes were due only to the positioning of the transducer relative to the seed.
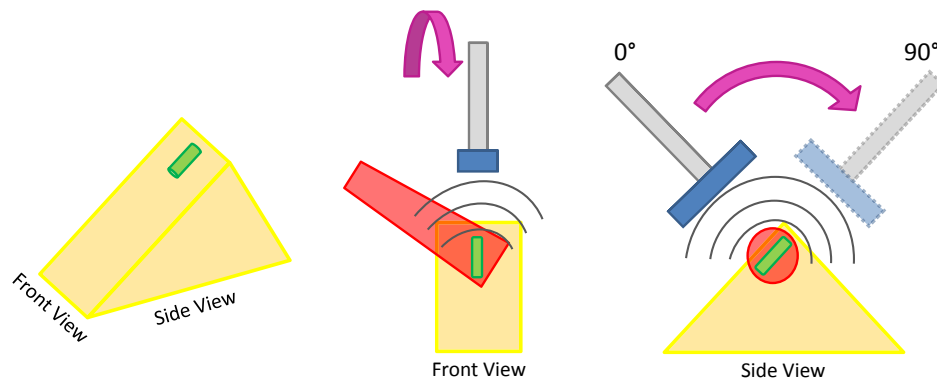


Fig. 2. Schematic representation of 3D phantom (left) and front (center) and side (right) view of transducer rotation apparatus. Yellow triangle/rectangle represents gelatin background; green ellipsoid, seed; blue and gray rectangles, transducer and mount, respectively. Red-shaded regions denote laser irradiation, while black lines represent acoustic transmission, both of which are oversimplifications and included for illustration purposes only. Purple arrow indicates transducer rotation axis.

In a second experiment (i.e., the "bare seed spectrum experiment"), the spectrum of a bare seed's PA signal was established. A non-reactive seed was embedded in a block of 8% gelatin and centered in the imaging plane with US imaging (using the aforementioned system/transducer). PA images of the seed were then obtained from 750 to 1090 nm in 20-nm increments, including 1064 nm. The extinction spectrum of the gelatin alone was analyzed using a UV-VIS-NIR spectrophotometer (UV-3600, Shimadzu Corp., Kyoto, Japan) and found to not significantly influence multi-wavelength PA imaging within the spectrum utilized for testing.

A third experiment (i.e., the "prostate tissue experiment") was performed to examine PAUS

imaging of brachytherapy seeds in a more realistic environment. In this experiment, five seeds were embedded into five excised bovine prostate samples, which were imaged within 24 hours of each animal's sacrifice, were never frozen, and were cut to be cubical in shape. The proximal tip of each seed was buried approximately 1 mm below the surface of the tissue at varied distances away from each sample's edge (see white scale in Fig. 3(a)). Each prostate sample was then cast in gelatin to prevent tissue discoloration or deterioration due to water immersion. The first of the five samples was oriented so that the seed's long axis was perpendicular to the US transducer face ("Short-axis Orientation" in Fig. 3(b)). This orientation was chosen to provide a minimum irradiation path through the prostate tissue of 1 mm, a depth that was too shallow to achieve in the long-axis orientation. For this comparison, multi-wavelength PA imaging, from 750 to 1090 nm, was performed. The other four samples were then oriented so that the seed's long axis was positioned parallel to the US transducer face ("Long-axis Orientation" in Fig. 3(b)). Using US visualization, the depth of each seed from the sample's edge was determined. Four irradiation path lengths were investigated - 4, 10, 13, and 17 mm - while PA images were acquired from 750 to 1090 nm in 40-nm increments, including 1064 nm. Note that PA and US beams were orthogonal to one another and were made to penetrate comparable depths into the tissue (i.e., when the irradiation path was increased, the US propagation path was increased accordingly).

For the second and third experiments, laser irradiation was delivered using an air beam directed at the seed. In all experimentation, laser fluences were measured for each imaging trial, and the mean ($n = 500$ pulses) energy was used to normalize the PA amplitude. Standard deviation of the laser fluence was also used to calculate standard error in the PA amplitude at each wavelength.



Short-axis Orientation          Long-axis Orientation

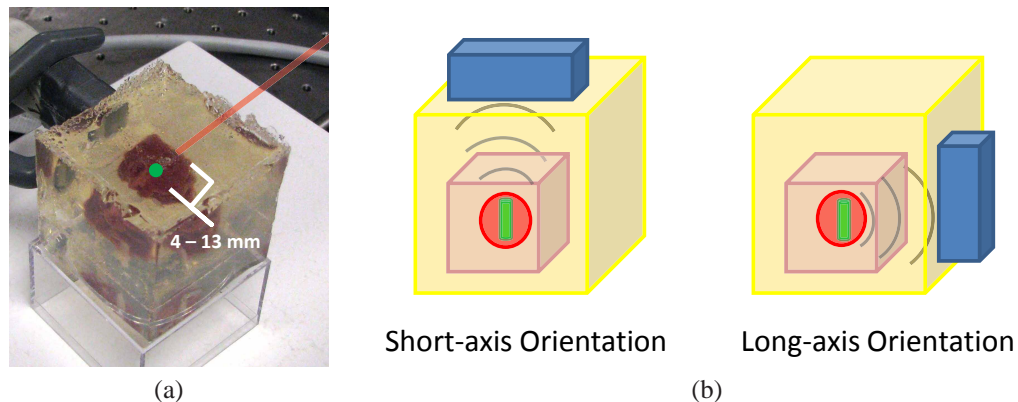(a)                                  (b)

Fig. 3. Picture of prostate sample cast in gelatin (a) and schematic views of imaging orientations (b). In picture of sample (a), green dot denotes approximate placement of seed (long-axis perpendicular to table), red line indicates example irradiation path, while US transducer is visible in upper-left portion of image (with aperture oriented perpendicular to table). White scale indicates varied distance of seed from front-most sample edge. In schematic depictions (b), short- (left) and long-axis (right) orientations are offered. Peach cube depicts embedded prostate sample; other conventions are same as used in Fig. 2.

For quantitative analysis, PA signal energies were calculated using a kernel surrounding the maximum signal from the seed. The kernel was determined by choosing a region of interest (ROI) with pixel values above a certain threshold in the B-mode image, which corresponded to the location of the seed. This region could be visually verified as the location of the seed due to the presence of the comet-tail artifact, which is present in US imaging of metals, that

was located distally from the aforementioned ROI. Data points within the kernel were averaged and normalized according to the mean laser fluence obtained during each trial. For contrast calculations, data kernels (0.6 x 0.4 mm) for the signal and background ROIs were chosen in order to obtain kernels containing only the respective signal and background measurements. The size of the kernel did not significantly affect contrast calculations as long as each kernel only contained these signal or background measurements. Several contrast values were obtained by translating the position of the signal kernel through the region of the seed (identified by the US image); a corresponding background kernel was similarly translated through an adjacent tissue region located outside the region of the seed. These values were then averaged together to obtain a single reported contrast value in US imaging and at each imaging wavelength in PA imaging. Contrast was calculated using:

$$\text{Contrast} = \frac{\overline{S_s} - \overline{S_b}}{\overline{S_b}}, \tag{1}$$

where $\overline{S_s}$ and $\overline{S_b}$ are the mean signals from a region within the seed and adjacent background, respectively.

## 3. Results

In the angular dependence experiment, PAUS images of the brachytherapy seed were acquired from 0° to 90°, in 15° increments. In both the PA and US images, the seed remained visible as the transducer was rotated. In the US images (grayscale images in Fig. 4), when the seed was oriented at 0° relative to the horizontal, the entire seed was visible. A large comet-tail artifact was also visible due to reverberation of the acoustic signal within the seed. As the transducer was rotated, the acoustic signal weakened from the midsection of the seed, while the distal and proximal tips of the seed remained apparent. Through the full rotation, the peak US signal decreased by 13%, with the majority of that decrease occurring between 0° and 30°.

Similar results were observed in the PA images of the seed (yellow-red colormap images in Fig. 4), where the 0° orientation offered the best visualization of the full seed. The body of the seed was still visible when rotated to an angle of 15° from the transducer; however, the signal diminished dramatically after that, as seen in rotation angles of 30° and greater. Much like the US images, comet-tail artifacts are present in the PA images. Unlike the US imaging results, however, only the proximal tip of the seed was clearly apparent through the full rotation of the transducer. Through the full rotation, the peak PA signal decreased by 46%, with the majority of that decrease occurring between 15° and 30°.

In the bare seed spectrum experiment, a seed embedded in pure gelatin was imaged with multi-wavelength PA imaging in order to determine the PA spectrum of the seed alone (red square in Fig. 5(a)). The normalized PA signal was plotted with respect to wavelength. The calculated spectrum presented a monotonically decreasing PA signal with increased laser wavelength, with an approximately 80% reduction in PA signal from 750 to 1090 nm.

The third experiment involved inserting non-reactive seeds into excised bovine prostate tissue. Figure 5(a) (blue circle) offers the PA spectrum of the seed shallowly embedded (short-axis orientation) in prostate tissue. Although the normalized PA signal tends to decrease with wavelength much like the bare seed (red square in Fig. 5(a)), local minima in signal are observed from 950 to 1010 nm, while a local maximum is observed at 1050 nm. Figure 5(b) shows the contrast spectrum for this seed in the short-axis orientation, with a peak (average) PA contrast of 40.1 dB (at 810 nm) compared to an average US contrast of 14.3 dB. Figure 6 shows the PAUS images obtained in the long-axis orientation from the 4-mm imaging depth. In the US image (Fig. 6(a)), background speckle is visible throughout the prostate tissue, with the proximal tissue-gelatin boundary clearly visible at 1.2-1.5 cm axially and the sample's edge visible at
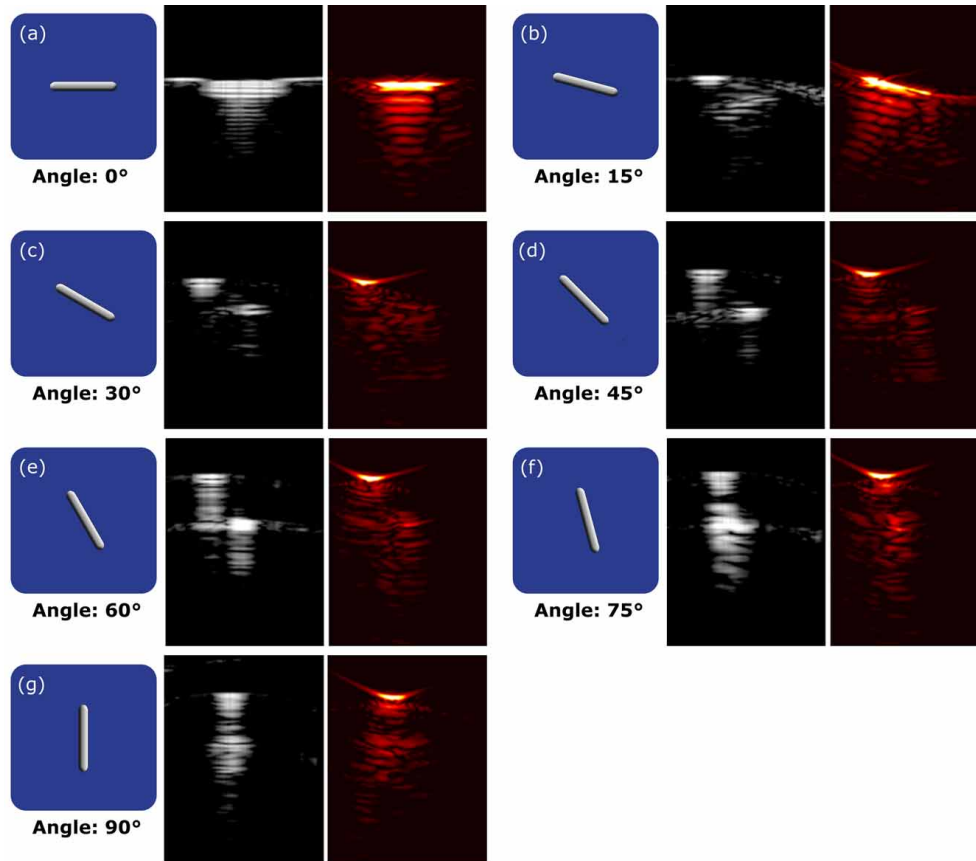
Fig. 4. US and PA images of brachytherapy seeds at different rotation angles relative to transducer face. Seed schematics (blue background) denote orientation, while first image immediately right offers US B-mode depiction (grayscale) and second image offers PA imaging depiction (yellow-red colormap). PA and US images are displayed with a 30-dB dynamic range, while all images (including schematic) are presented with same scale (i.e., seed is 0.8 x 4.5 mm) and co-registered orientations/positions. Transducer face is located/aligned with top margin of schematic.

the 4-mm lateral position. Although a hyperechoic region is visible at the seed location (i.e., 2.4 cm), the speckle signal from the surrounding tissue reduces overall contrast. A PA image (Fig. 6(b)) obtained at the same position presents a strong acoustic signal from the seed location, but little acoustic signal is present in the surrounding tissue, resulting in a significant improvement in contrast. By combining Figs. 6(a) and 6(b), the co-registered images (Fig. 6(c)) are able to more clearly display the presence of the brachytherapy seed within the tissue background.

Lastly, the seed was successfully imaged with three different irradiation path lengths, and the PA signal spectrum of each was calculated at ten wavelengths (Fig. 7(a)–7(c)). Note that the seed could not be visualized at 17 mm with the utilized fluences, which were similar to those used for imaging at the three shallower depths. For the other three depths (i.e., 4, 10, and 13 mm), a local maximum of the normalized PA signal exists at 1064 nm, while a local minimum can be observed at 990 nm. PA amplitudes for the 10-mm (b) and 13-mm (c) acquisitions decreased, on average, by 93% and 94%, respectively, when compared to the average
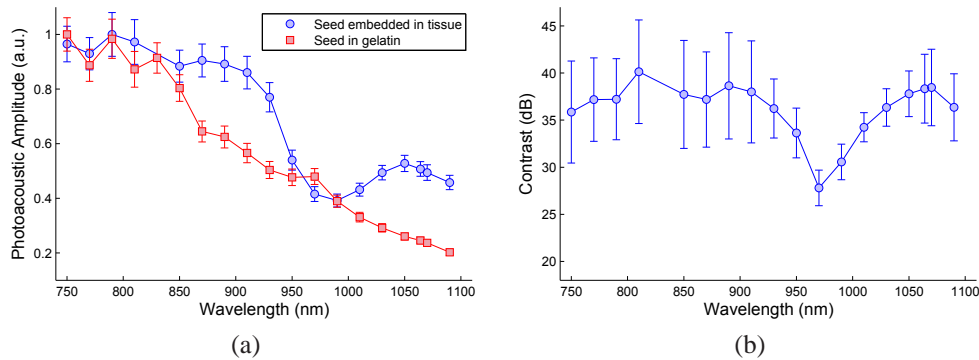
Fig. 5. Normalized PA signal of seed embedded in gelatin (a - red square) and embedded in excised bovine prostate (a - blue circle) and contrast spectrum of seed embedded in prostate sample (b). Proximal end of seed is embedded approximately 1 mm from prostate tissue surface (in direction of laser source). Note for the prostate tissue experiment (i.e., blue circle), data file obtained at 830 nm was corrupt and was thus omitted from analysis.

PA amplitude of the 4-mm (a) acquisition. Figure 7(d)–7(f) presents the contrast values across the acquired spectrum for the three imaging depths. Peak (average) PA contrasts were 50.6 dB (at 870 nm), 30.3 dB (at 830 nm), and 28.2 dB (at 1064 nm), while average US contrasts were 22.7 dB, 24.7 dB, and 25.5 dB for the 4-mm, 10-mm, and 13-mm acquisitions, respectively. Surface fluences were measured (mean$\pm$SD) across the acquired spectrum to be $21.7\pm2.3$, $23.6\pm3.1$, and $22.5\pm5.1$ mJ/cm$^2$ for the 4-mm, 10-mm, and 13-mm acquisitions, respectively; fluences tended to decrease with increased wavelength. Specifically, at a wavelength of 1064 nm, surface fluences were measured to be $19.7\pm0.9$, $21.3\pm0.9$, and $20.1\pm0.8$ mJ/cm$^2$ for the aforementioned acquisition depths, respectively.

## 4. Discussion

PA imaging of brachytherapy seeds embedded in prostate tissue yielded an improvement of at most 27.9 dB in contrast over conventional US imaging, while seeds were successfully visualized at depths of up to 13 mm. Much like US imaging, PA imaging results were dependent on seed orientation. As the PA images provided no anatomical context due to their inherently poor soft tissue contrast, a combined PAUS imaging technique appears necessary for future clinical application.

In the angular dependence experiment, US imaging results are similar to those observed by Davis *et al.*, with the 0° orientation affording the greatest and most uniform acoustic signal [6]. This orientation maximizes the seed's surface area that is perpendicular to and within the path of the acoustic wave transmission, which maximizes backscattered energy. Because the seed becomes an acoustic source when excited by the PA effect, PA imaging yielded very similar rotation results. Due to the seed's capsular geometry, the directivity pattern of the acoustic energy emanating from the seed yields the greatest energy at points normal to the seed's cylindrical midsection. If evenly irradiated, acoustic energy will radiate outward from the seed body. This explains why only the proximal tip of the seed is well visualized in PA imaging as the distal tip, which is rotated away from the transducer face, will tend to transmit energy in the opposing direction.

In the bare seed spectrum experiment, the PA signal spectrum of a bare seed was found to monotonically decrease with increasing laser wavelength. Although the tested wavelength
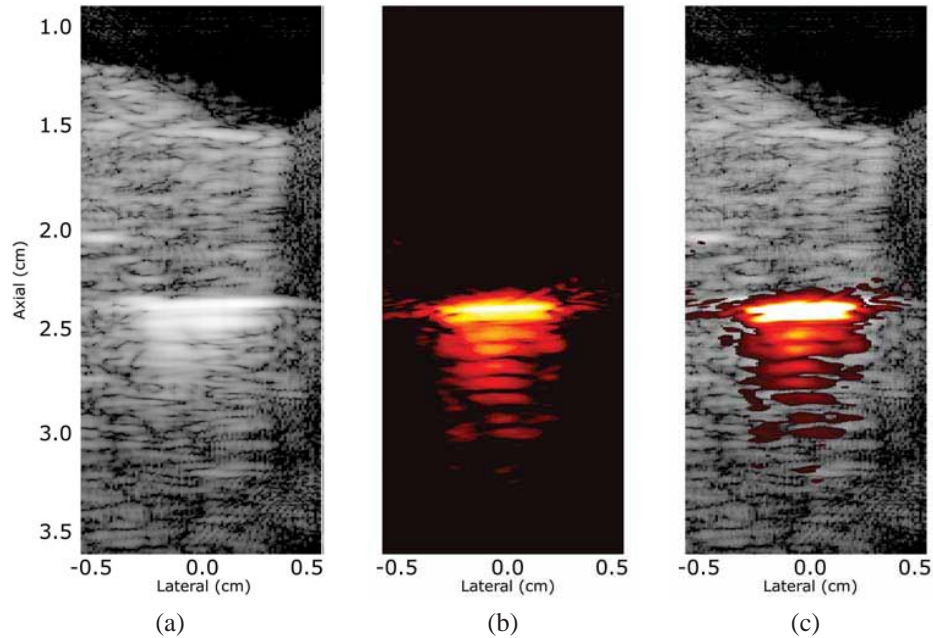
Fig. 6. US B-mode (a), PA (b), and combined PAUS (c) images of a seed embedded in a bovine prostate sample in the long-axis orientation. PA image was acquired at 870 nm and is displayed with 35-dB dynamic range; B-mode image is displayed with 55-dB range.

range extended beyond that covered in Fig. 1, the general trend of decreased absorption with increased wavelength observed in the spectrum for chromium-oxide (solid turquoise line) is consistent with the similar decrease in PA signal - which is proportional to optical absorption - observed in this study. When the seed was shallowly embedded in prostate tissue, however, the generated PA signal spectrum has local minima from 950 to 1010 nm. The phenomenon seen here is likely related to the "environmental" effect of the surrounding tissue (optical) properties on the seed's PA signal. Though the PA signal amplitude is directly related to the optical absorption coefficient of the metallic seed, local fluence is also dependent on the optical absorption and scattering coefficients of the surrounding tissue, resulting in a nonlinear dependence of the PA signal on tissue properties.

In the depth dependence results, contrast plots (Fig. 7(d)–7(f)) were found to have local maxima at 1064 nm, with the deepest acquisition (13 mm) having its absolute maximum at this wavelength as well. Such a result is counter to what the results in the bare seed spectrum experiment might suggest should occur (i.e., given that the PA signal was greatest at 750 nm for the bare seed). In studies of human prostate, scattering has been identified as the dominant loss mechanism and has been found to decrease with increasing irradiation wavelength; this is typical for most soft tissues [16]. Though the optical absorption of metal also decreases with increasing wavelength, the reduction of this absorption with increased wavelength is likely more modest than the decrease in local fluence that results from scattering at lower wavelengths. Given that the obtained PA signal is directly proportional to both optical absorption and local fluence, increasing imaging depth - which reduces local fluence but has no effect on optical absorption - appears to favor higher wavelengths. A local minimum in all of the spectra is observed at 990 nm, a phenomenon which is consistent with the more finely sampled spectrum (blue circle in Fig. 5(a)) acquired for the shallowly embedded seed and is likely a consequence
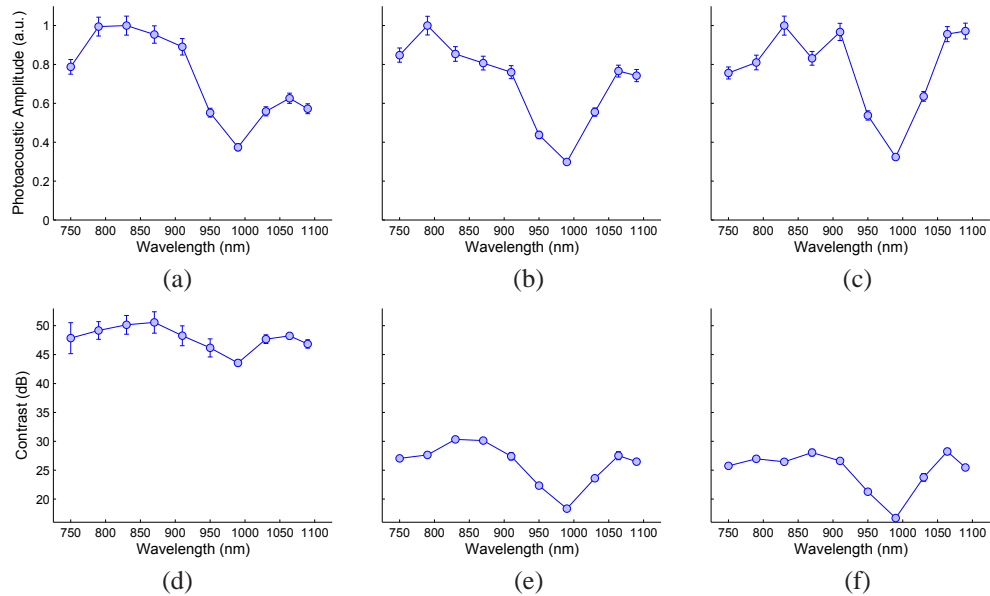
Fig. 7. Normalized PA spectra and contrast of brachytherapy seed embedded in bovine prostate at three laser irradiation depths: 4 mm (a,d), 10 mm (b,e), and 13 mm (c,f).

of the trade-off between the absorption/scattering properties of the prostate tissue and the decreasing absorption of metal with increasing wavelength.

Contrast values obtained from the PA images of the seed in prostate tissue (Figs. 5(b) and 7(d)–7(f)) highlight the importance of local fluence and seed orientation on seed visualization. Firstly, a significant decrease in contrast was observed from the 4-mm imaging depth (50.6 dB) to the 10-mm and 13-mm imaging depths (30.3 dB and 28.2 dB, respectively). This decrease is likely due to the drastic reduction in local fluence that results from increased scattering occurring through deeper interrogation regions; this notion is supported by over 90% reductions in PA signals for these deeper interrogations despite surface fluences that were comparable to those used for the shallower, 4-mm interrogation. Additionally, contrast appears to be affected by seed orientation. For the shallowly embedded seed that was imaged in the short-axis orientation (Fig. 5(b)), a 10.5-dB reduction in peak contrast was observed between it and the 4-mm, long-axis orientation (Fig. 7(d)). This reduction is due in large part to the nearly 50% reduction in PA signal experienced with the rotation of the brachytherapy seed. Such a signal reduction - which also occurs but to a lesser extent for US imaging - would have resulted in US imaging slightly outperforming PA imaging (i.e., with theoretical contrasts of 24.3 dB and 22.9 dB, respectively) for the 13-mm acquisition had the seed been imaged in the short-axis orientation. For the 4-mm acquisition, theoretical contrast calculations suggest that PA imaging would have still outperformed US imaging had the seed been imaged in the short-axis orientation, with a slightly reduced contrast improvement (i.e., PA imaging over US imaging) of 24.4 dB (compared to a 27.9-dB improvement) being realized in this case. A study by Corbett *et al.* found, however, that the majority of seeds are placed approximately parallel (i.e., $\pm 16°$) to the transducer face during a clinical procedure [20]. Thus, although the case of short-axis imaging is an important one to consider, seeds tend to be oriented for optimal PA imaging. Ultimately, to obtain an appreciable contrast gain in any orientation and fully realize PA imaging's potential in this application, adequate local fluence at the seed location must be achieved.

As previously noted, it was not possible to image a brachytherapy seed at a depth of 17 mm in the prostate tissue sample due to insufficient local fluence. In an effort to increase local fluence in a clinical setting, a fiber optic-based light delivery system could be introduced through a patient's urethra. This would provide an additional irradiation source from within the tissue. With the urethra running through the prostate, maximum irradiation path lengths would be on the order of the prostate's radius (i.e., half the width or height dimension), which was found to have a mean of 21 mm in a study of men aged 52-67 years [17]. Consequently, as clinical application of this technology requires imaging beyond the 13 mm demonstrated herein, the use of higher energies and reduced tissue scattering at 1064 nm could be critical in an effort to achieve clinical utilization. In clinical settings, at 1064 nm the American National Standards Institute (ANSI) allows for maximum safe laser fluences of 100 mJ/cm$^2$ compared to 20 mJ/cm$^2$ at $\leq$700 nm when imaging through skin [18]. Although there is not currently a specific fluence regulation for irradiation through either the rectal or urethral wall, the aforementioned ANSI limit for skin is likely a conservative estimate for what would be allowed for this application given the relatively high absorption of skin (see Fig. 1). Based on this limit, a five-fold increase in surface fluence would be allowed in this study. Additionally, it might also be possible to increase local fluence by increasing the laser's pulse width. From a practical standpoint, the primary wavelength of an Nd:YAG laser is 1064 nm, making systems capable of imaging at this wavelength readily available and relatively inexpensive. The use of 1064 nm for molecular PA imaging is being pursued for similar reasons [19].

The rotation results from the first experiment demonstrate that PA imaging typically does not improve visualization of the full seed. When the seed is not approximately parallel to the transducer face, only the distal tip of the seed can be visualized with PA imaging, while both tips can be visualized with US imaging. The true improvement offered by PA imaging is in detecting and locating the seed, as evidenced by as much as a 27.9-dB increase in contrast. In a study by Corbett *et al.*, it was found that when multiple seeds are implanted, the placement of each seed is important in achieving the intended radiation dose distribution while the orientation is not [20]. Thus, PA imaging's enhanced capability of visualizing the location of seeds could improve a clinician's ability to implement a specific treatment plan.

One source of experimental error from this study could have resulted from the irradiation source. The assumption was made that the surface area of the seed facing the ultrasound transducer was irradiated evenly. This was difficult to achieve for two reasons. Firstly, due to the experimental setup, the irradiation source was placed off-axis, which is not optimal for irradiation alignment with the obliquely positioned transducer face. Secondly, generation of a homogeneous beam profile across the seed surface is difficult when relatively high fluences must be maintained. These experimental issues would have been exacerbated in the experiments utilizing pure gelatin as a background material, while the turbid environment of prostate tissue would have mitigated these effects. A second source of error could have resulted from the use of five different prostate samples. Although the use of different samples lends more significance to certain multi-wavelength results (e.g., the existence of local minima and maxima at approximately 990 nm and 1064 nm, respectively), it could have also resulted in different depth-dependent scattering between samples.

## 5. Conclusion

PA imaging promises improved contrast of brachytherapy seeds in tissue, yielding improvements ranging from 2.7 to 27.9 dB in contrast over US imaging alone for seeds in the long-axis orientation and for imaging depths ranging from 4 to 13 mm. Even more drastic than in US imaging, there is an angular dependence of a seed's PA signal, with the orientation having the greatest surface area normal to the acoustic beam direction resulting in the greatest PA signal.

To achieve significant contrast improvements in a clinical application, which would call for imaging depths around 20 mm if a dual transurethral-transrectal irradiation source were implemented, greater laser energies at increased wavelengths (e.g., 1064 nm) will likely need to be utilized to obtain adequate local fluences. Nonetheless, combined PAUS imaging shows strong promise in accurately visualizing the seed and surrounding tissue anatomy during brachytherapy seed placement procedures.

## Acknowledgments